PHYSICAL REVIEW FLUIDS **6**, 074701 (2021)

Cascades and reconnection in interacting vortex filaments

Rodolfo Ostilla-Mónico,[1] Ryan McKeown ,[2] Michael P. Brenner,[2]
Shmuel M. Rubinstein ,[3] and Alain Pumir [4,5]
[1]*Department of Mechanical Engineering, University of Houston, Houston, Texas 77204, USA*
[2]*School of Engineering and Applied Sciences, Harvard University, Cambridge, Massachusetts 02138, USA*
[3]*The Racah Institute of Physics, The Hebrew University of Jerusalem, Givat Ram, Jerusalem 91904, Israel*
[4]*Université de Lyon, ENS de Lyon, Université Claude Bernard, CNRS, Laboratoire de Physique, 69342 Lyon, France*
[5]*Max Planck Institute for Dynamics and Self-Organization, 37077 Göttingen, Germany*

(Received 22 February 2021; accepted 22 June 2021; published 7 July 2021)

The reconnection of two interacting vortex tubes is a fundamental process in fluid mechanics, which, at very high Reynolds numbers, is associated with the formation of intense velocity gradients. Reconnection is usually studied using two antiparallel tubes which are destabilized via the long-wavelength Crow instability, leading to a very symmetric configuration and to a strong flattening of the cores into thin sheets. Here, we consider the interaction of two initially straight tubes at an angle of β and show that by relaxing some symmetries of the problem, a rich phenomenology appears. When the angle between the two tubes is close to $\beta = 90^\circ$, their interaction leads to pairing of small portions of antiparallel tubes, followed by the formation of thin and localized vortex sheets as a precursor of reconnection. The subsequent breakdown of these sheets involves a twisting of the paired sheets, followed by the appearance of a localized cloud of small-scale vortex structures. By decreasing β, we show that reconnection involves increasingly larger portions of tubes, whose cores are subsequently destabilizing, leaving behind more small-scale vortices. At the smallest values of the angle β studied, the two vortices break down through a mechanism, which leads to a cascadelike process of energy conveyance across length scales similar to what was found for previous studies of antiparallel vortex tubes ($\beta = 0$) which imposed no symmetries. While, in all cases, the interaction of two vortices depends on the initial condition, the rapid formation of fine-scale vortex structures appears to be a robust feature, possibly universal at very high Reynolds numbers.

DOI: 10.1103/PhysRevFluids.6.074701

I. INTRODUCTION

Many experiments have demonstrated that the interaction of two vortex tubes coming close together eventually leads to a change of topology of the vortex lines through a process known as vortex reconnection [1–3]. Vortex reconnection is a fundamental process in fluid mechanics, and it has been postulated to play a significant role in fluid phenomena such as the turbulent energy cascade [4], noise generation [5], and the transfer of helicity across topologically distinct vortices [6]. Reconnection is also interesting from a theoretical point of view, as the change of vortex line

---

topology appears to violate well-known conservation theorems in inviscid flows [7], which implies that viscosity must play a decisive role even at extreme Reynolds numbers.

The process through which vortex pairs undergo reconnection has been well studied and characterized both numerically and theoretically. The early phase of the interaction, before viscosity plays the dominant role, is captured by the Biot-Savart equation, which keeps track of the location of the vortex tubes by assuming a circular structure of the cores, with a fixed vorticity profile [8]. The numerical work of [9] showed that the resulting dynamics of a wide range of initial conditions spontaneously leads to the local pairing of antiparallel parts of nearby filaments. As a result, the cores get close together, which generally leads to very rich dynamics. The Biot-Savart description, however, fails when the vortex tubes are so close that they deform each others' cores, thereby making the initial assumption questionable [10,11]. Therefore, to adequately capture the initial dynamics of the interaction, it is necessary to undertake a full simulation of the Euler equations, even if neither the Biot-Savart equation nor the Euler equations capture any of the viscous processes essential to reconnection.

It has been known for a long time that several instability mechanisms may lead to the disruption of two antiparallel vortex lines. Early studies based on the Biot-Savart equation suggested that the long-wavelength Crow instability [12] plays the dominant role in bringing together counter-rotating parts of the tubes so reconnection can occur [13,14]. This prompted a number of investigations (see, e.g., [5,15–20]), based on numerical solutions of the Euler and Navier-Stokes equations which imposed the symmetry of the most unstable mode corresponding to the long-wave-number Crow instability, in particular a mirror symmetry with respect to the plane that separates the two tubes (denoted as the plane P_2; see further detail in Sec. II). When this symmetry is imposed, the components of velocity perpendicular to the plane P_2 are uniformly zero, meaning that if the vorticity component perpendicular to the plane is zero, reconnection is impossible in the absence of viscosity.

The study of simplified models, based on the Biot-Savart equations, has clearly shown that antiparallel filaments pair [9] and subsequently amplify each other in a singular manner, although the approximations justifying the use of Biot-Savart ultimately break down [13,21,22]. Many careful studies have been devoted to the amplification of velocity gradients when two vortex tubes interact. In the inviscid limit, the attempts to find signs of a diverging vorticity have not led to unambiguous answers [15,17,18]. Still, direct numerical simulations (DNS) clearly show that very thin vortex sheets are formed on either side of the symmetry plane P_2, both in the inviscid and in the viscous problem at large enough Re_Γ. In all these studies, the formation of extremely thin vortex sheets, with a relatively slow growth of vorticity, makes the problem very difficult to study numerically.

While the quest to reach increasingly large values of Re_Γ continues [23], numerical and experimental studies have recently identified another main mechanism in the interaction between two antiparallel tubes, which leads to the breaking of the vortex tubes following a different scenario [24]. This mechanism can be observed in the head-on collision between two vortex rings, which leads to a very rapid destruction of the vortices at large Reynolds numbers [25]. In this problem, the long-wavelength Crow instability initially brings parts of the filaments together [26,27]. However, the further interaction between the counter-rotating tubes reveals the dominant role of an instability whose wave number is comparable with the core size [28,29]. This instability, known as the elliptic instability [26,30,31], involves a symmetry that completely differs from that of the long-wave-number Crow instability. At sufficiently high Reynolds numbers, elliptic instabilities develop on top of each other, leading to a cascade and eventually to a transient turbulent flow [24].

The marked difference between these two cases leads us to investigate the onset of the mechanisms leading to reconnection. In this vein, we take inspiration from the studies of reconnecting magnetic tubes at an angle in an astrophysical context [32], and from the recent study of vortex reconnection in superfluids, which has revealed the presence of nonuniversal features by comparing different classes of initial conditions [33]. However, we have to highlight the notable difference between these two cases, and ours, which arises from much larger degrees of freedom of the vortex cores in hydrodynamics and leads to a much richer phenomenology, not taken into account in the simplified model of reconnection of skewed vortices in [34]. While it is clear that reconnections are still present in hydrodynamical fluids with $\mathrm{Re}_\Gamma \gg 1$ [23], their appearance could be restricted to a rather small subset of initial conditions that either enforce many symmetries on the vortices or stabilize the core through spin [20], as simulations have shown the long-range interaction between vortices tends to align them in an antiparallel manner [9,35]. This would mean that reconnections (understood as topological changes) could become rarer in classical fluids than in idealized models, even if they remain important in the former case from a theoretical and mathematical perspective [36].

We address these question about genericity and universality by relaxing some of the strict symmetries imposed on the usual reconnection studies. We perform a series of direct numerical simulations which use the simple configuration of two counter-rotating vortex tubes oriented at an angle as the initial condition. We work at a Reynolds number where, for antiparallel tubes, the elliptical instability dominates due to the amplification of strain that results from their alignment. We start off with two filaments which are perpendicular to each other. For this configuration, we will see that the strain orientation does not excite the elliptical instability. We then vary the angle, making the vortices more antiparallel and recover the elliptical instability. In practice, we use $b = \cot(\beta/2)$, where β is the angle between the filaments. With this choice, $b = 1$ corresponds to two initially perpendicular filaments: $\beta = \pi/2$. In this study, we consider only values of $\beta \leqslant \pi/2$ ($b \geqslant 1$), thus favoring configurations where the two filaments tend to be initially counter-rotating, rather than corotating. We note that the configuration $\beta = \pi/2$ ($b = 1$) has been studied, originally at much smaller Reynolds numbers than the ones considered here and with an additional hyperviscous dissipation term [37], and, more recently, at a much higher resolution [38].

In all cases, we find an energy cascade during the interaction, reaching ever smaller scales as the Reynolds number increases. This generation of small scales arises from deformations of the cores where the tubes intersect. We find that the interaction starts with the formation of characteristic vortex sheets for $67.4^\circ \leqslant \beta \leqslant 90^\circ$ ($1 \leqslant b \leqslant 3/2$). For $\beta \leqslant 53.1^\circ$ ($b \geqslant 2$), however, the mechanism that prevails in the interaction between the two tubes is the formation of transverse vortex tubes, as observed, formally, when $\beta \to 0$ ($b \to \infty$) due to the presence of the elliptical instability [24].

II. NUMERICAL PROCEDURES AND DATABASE

We simulate the incompressible Navier-Stokes equations:

$$\partial_t \boldsymbol{u} + (\boldsymbol{u} \cdot \nabla)\boldsymbol{u} = -\rho^{-1}\nabla p + \nu \nabla^2 \boldsymbol{u}, \tag{1}$$

$$\nabla \cdot \boldsymbol{u} = 0, \tag{2}$$

in a triply periodic box, using pseudospectral methods. The details of the code have been described in [39]. We vary the aspect ratio of the domain, which we take to be of size 2π in the x and y directions, and of size $2b\pi$ in the z direction, where b is a control parameter that we take as $b =$ 1, 5/4, 3/2, 2, 5/2, 3, and 4. No forcing is added to the Navier-Stokes equations and the flow is allowed to evolve from the initial conditions. These consist of two Gaussian vortices, where the initial position of the vortex cores is in two diagonal lines $\gamma_\pm$: $z = \pm bx$ located at the plane $y = \pm d/2$. The vorticity is initially concentrated around the two lines, with a Gaussian distribution: $\boldsymbol{\omega}_\pm(\boldsymbol{x}, t = 0) = \pm\Omega \exp(-\boldsymbol{\rho}_\pm^2/2\sigma^2)(\boldsymbol{e}_x \pm b\boldsymbol{e}_z)/\sqrt{1 + b^2}$, where $\boldsymbol{\rho}_\pm$ is the distance between the point $\boldsymbol{x}$ to the two lines $\gamma_\pm$, and σ is the core radius. The resulting circulations $\Gamma_\pm$ are equal to $\Omega\sigma^2$. A schematic of the initial condition can be seen in Fig. 1, which shows that the isocontours of vorticity approximately concentrate in two tubes, at an angle of inclination $\beta = 2\arctan(1/b)$, consistent with the periodicity of the box. By construction, the two tubes are at a minimal distance from each other at the center of the box, (0,0,0). Additionally, the periodicity of the solution imposes that the two tubes are also very close at $(\pi, 0, b\pi)$ [or, equivalently, at $(-\pi, 0, -b\pi)$] and, in fact, at points deduced by periodicity from these two positions, as shown in the Supplemental Material [40]. It is

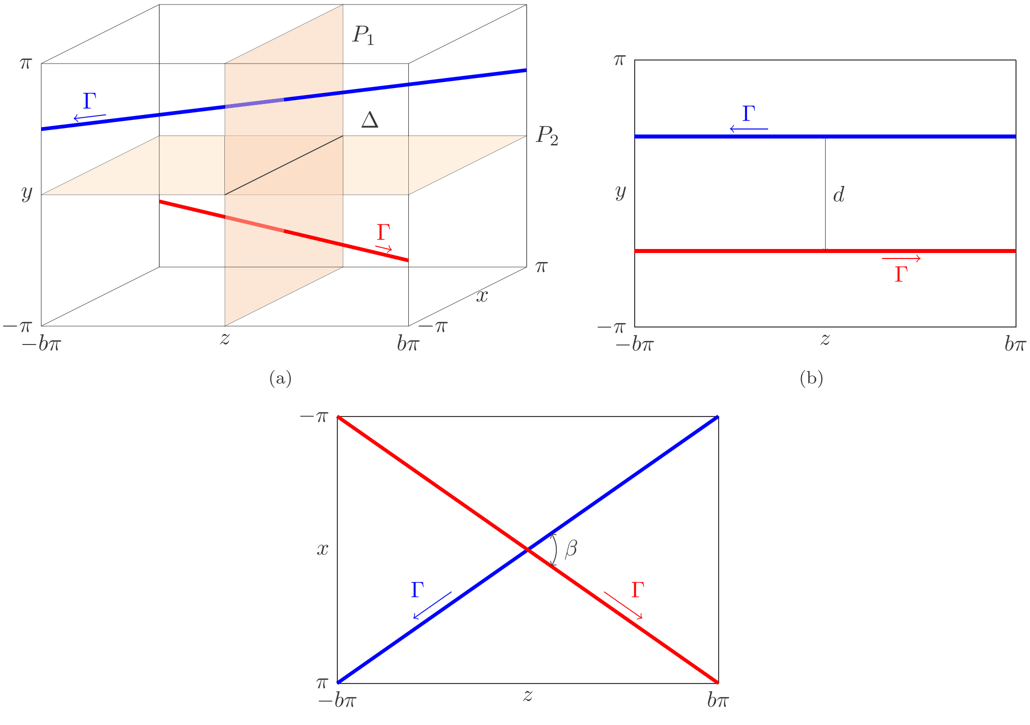

(a)

(b)

(c)

FIG. 1. Schematic of DNS initial configuration. The thick red and blue lines represent the initial positions of the two vortex filaments, with the arrow indicating the circulation direction. (a) Three-dimensional (3D) schematic. (b) Side view of the yz plane, which shows the definition of the spacing between the filaments, d. (c) Top view of the xz plane, which shows the definition of β and b. The vorticity distribution is invariant under the symmetry resulting from two mirror symmetries with respect to the planes P_1 and P_2: $(x, y, z) \to (x, -y, -z)$, $(\omega_x, \omega_y, \omega_z) \to (\omega_x, -\omega_y, -\omega_z)$, and $(u_x, u_y, u_z) \to (u_x, -u_y, -u_z)$. The distance between the two tubes in the y direction is $d = 0.9$; the circulation is chosen here to be $\Gamma = 1$, and the core radius $\sigma = 0.4/\sqrt{2} \approx 0.28$.

sufficient to study the strong interaction between the two tubes occurring at the center of the box. We focus on this point in the following.

In all the calculations presented here, we have taken $\Gamma = 1$, $d = 0.9$, and $\sigma = 0.4/\sqrt{2} \approx 0.28$. The Reynolds number Re_Γ has been varied by changing the viscosity ν. Our calculations are organized in two series of runs. In the first series, we fix the angle by setting $b = 1$, which results in tubes at $\beta = 90^\circ$ to each other. This configuration minimizes the strain direction that triggers the elliptical instability. We then vary the Reynolds number, from $\mathrm{Re}_\Gamma = 2200$ to $\mathrm{Re}_\Gamma = 5400$, which is around the Reynolds number range for which the elliptical instability supersedes the Crow instability for antiparallel tubes [26,41], to study the genericity of the elliptical instability in the most disadvantageous configuration. In the second series of runs, we fix the Reynolds number at $\mathrm{Re}_\Gamma = 4000$, and vary b from 1 to 4, which reduces the angle β and brings the tubes closer to being antiparallel, progressively amplifying the strain in the direction that induces the elliptical instability.

In addition, we considered three runs, i.e., runs 12A–12C, with initially antiparallel vortex tubes, in the configuration studied in [24,27]. These runs were carried out in a box of aspect ratio 4, although they correspond formally to $\beta = 0$, hence $b \to \infty$, at the fixed Reynolds number $\mathrm{Re}_\Gamma = 4000$. When initializing the flow, we slightly modulated the constant x and y locations of the tubes by a sum of a few Fourier modes. Starting from a value of the perturbation for run 12A, we divided

TABLE I. Simulation parameters for the runs used in this work. The numerical domain is taken as $-\pi \leqslant x \leqslant \pi$, $-\pi \leqslant y \leqslant \pi$, and $-b\pi \leqslant z \leqslant b\pi$. The Reynolds number is defined as the ratio of the initial circulation Γ divided by the kinematic viscosity ν. Each run was started at low resolution, with $N_l \times N_l \times bN_l$ Fourier modes. The runs were also conducted at a higher resolution, with $N_h \times N_h \times bN_h$ Fourier modes during the generation of small-scale flow structures. In the case of runs 12A–12C, corresponding to $\beta = 0^\circ$, the limits in the z direction are taken as $-4\pi \leqslant z \leqslant 4\pi$, and the z resolution* is, accordingly, $4N_l$ or $4N_h$.

Runs	1	2	3	4	5	6	7	8	9	10	11	12A/B/C
b	1	1	1	1	1	5/4	3/2	2	5/2	3	4	∞
β	90°	90°	90°	90°	90°	77.3°	67.4°	53.1°	43.6°	36.8°	28.1°	0°
Re_Γ	2200	3300	4000	4550	5400	4000	4000	4000	4000	4000	4000	4000
N_l	256	256	384	384	384	192	240	192	192	192	192	192*
N_h	384	512	512	512	512	384	400	320	320	320	320	320*

the amplitude of the perturbation by 2 (run 12B) and by 4 (run 12C). The runs were carried out at low resolution ($192^2 \times 768$). To judge the resolution of our runs, we compared several statistics obtained from our runs at low resolution ($N = N_l$) with the run at higher resolution ($N = N_h$), as discussed in the text. In the case of the run at $\beta = 0^\circ$, i.e., run 12A, these tests convinced us that the low resolution is sufficient.

Additionally, Fig. 13 shows the energy spectra for a few runs, in the time range where the resolution requirements are the most stringent. This includes the run at the highest resolution, i.e., run 5 [$\mathrm{Re}_\Gamma = 5400$, $\beta = 90^\circ$, Fig. 13(a)], along with the two runs used to illustrate our results, namely, run 3 [$\mathrm{Re}_\Gamma = 4000$, $\beta = 90^\circ$, Fig. 13(b)] and run 11 [$\mathrm{Re}_\Gamma = 4000$, $\beta = 28.1^\circ$, Fig. 13(c)], as well as run 12A [$\mathrm{Re}_\Gamma = 4000$ and $\beta = 0^\circ$, Fig. 13(d)].

In all the runs, the initial evolution is relatively smooth and does not require a very high resolution. We have therefore started all the runs at a low resolution, with a grid of size $N_l \times N_l \times (bN_l)$ (or, equivalently, with as many Fourier modes). When the vortex tubes come together, the velocity field develops very fine scales or, equivalently, the Fourier spectrum extends to much larger values of the wave numbers k. To simulate this phase of the dynamics, we extend the number of Fourier modes to $N_h \times N_h \times (N_h b)$. The parameters of the various simulations are shown in Table I.

In the following, all quantities will be expressed in units defined with the box size and a unitary circulation. Note that the timescale associated with the inviscid evolution (Biot-Savart model) is $\sim d^2/\Gamma$, which is of the order of 1.

Symmetries of the problem. Although the planes P_1 ($z = 0$) and P_2 ($y = 0$), as indicated in Fig. 1, play a role in the problem studied here, the velocity and vorticity fields in our simulations do not have any simple symmetry with respect to P_1 or P_2. In configurations with a symmetry with respect to P_1, as is the case, e.g., in [11,15–20,42,43], the component of the velocity field perpendicular to P_1 is equal to 0 in P_1. As a consequence of this symmetry, if the component of vorticity perpendicular to P_1 is initially 0 in the symmetry plane P_1, then a component of vorticity perpendicular to P_1 cannot be generated without viscosity.

Conversely, there is no particular symmetry plane between two vortex tubes undergoing the elliptic instability [24,27] or in the configuration of two vortex tubes initially at a finite angle. Nonetheless, the fields in the present study are invariant after composing the two mirror symmetries with respect to P_1 and to P_2 or, equivalently, by a rotation with respect to their intersection, i.e., the straight line Δ ($z = y = 0$) shown in Fig. 1(a). This corresponds to the following symmetry:

$$(x, y, z) \to (x, -y, -z), \quad (u_x, u_y, u_z) \to (u_x, -u_y, -u_z), \quad \text{and} \quad (\omega_x, \omega_y, \omega_z) \to (\omega_x, -\omega_y, -\omega_z). \tag{3}$$

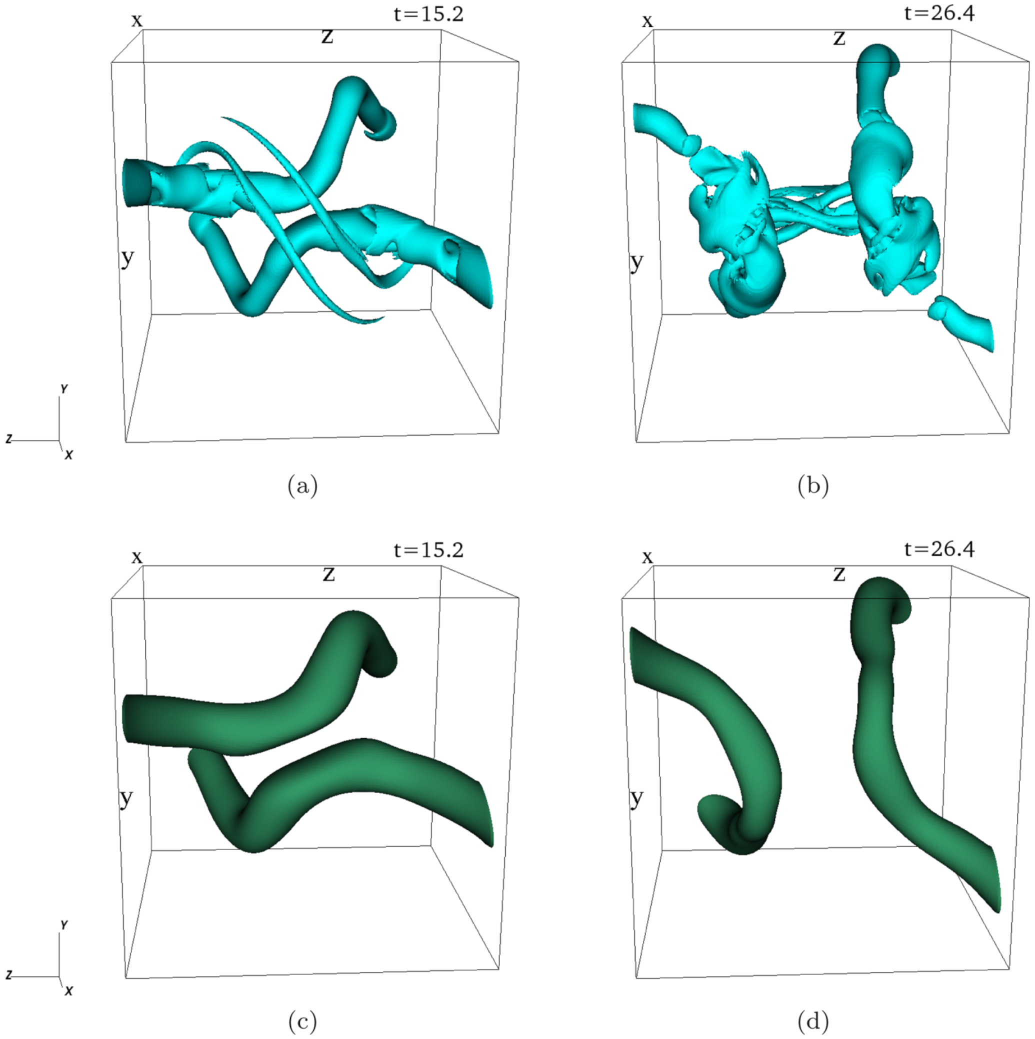

(a) (b)

(c) (d)

FIG. 2. Vortex topology changes during a reconnection between initially perpendicular vortex tubes ($b = 1$ and $\mathrm{Re}_\Gamma = 4000$, run 3 in Table I). (a),(b) In a subdomain of size $3.68 \times 3.68 \times 3.68$ around the center of the computational box, the isovorticity contours corresponding to $\omega_{th} = 2.5$ at $t = 15.2$, when the tubes begin to interact, and at $t = 26.4$, after the interaction. These dynamics reveal a change of topology of the vortex lines and the generation of small-scale vortices during the reconnection. (c),(d) The same vorticity field, bandpass filtered between $k_< = \sqrt{2}k_f$ and $k_> = 2\sqrt{2}k_f$, with $k_f = 2.3$, which removes the small-scale features of the flow and showcases only the change of topology of the vortex tubes. The value of the isosurface is 1 in (c) and (d). Full videos of the process are available in the Supplemental Material [40].

III. RESULTS

A. Overview of reconnection

We begin by illustrating the phenomenon of reconnection for initially perpendicular vortex tubes by analyzing run 3, with $\beta = 90^\circ$ ($b = 1$), $\mathrm{Re}_\Gamma = 4000$. Figure 2 shows isocontour surfaces of the vorticity field, with a value of the threshold ω_{th}, indicated in the captions, over a subdomain of the computational domain, centered at the point where the vortices interact, of size $[-1.84, 1.84]^3$. The evolution over the full computational domain is shown in Fig. 2 of the Supplemental Material [40].

In the computational domain, the vortices also strongly interact at another point, where the tubes are initially closest, near $(\pi, \pi, 0)$. The vortices evolve in time from the initial horizontal conditions, as they approach one another and begin to deform. Figure 2(a) shows the vorticity isosurface at $t = 15.2$, before reconnection. The two tubes, originally at an angle $\beta = 90^\circ$, are now antiparallel in the region of interaction [9]. As the flow evolves further, the vortices reconnect. This results in a changed topology, which can be inferred from the structure of the vorticity field shown in Fig. 2(b) at $t = 26.4$. Vertical vortex structures, however, appear simultaneously with smaller scale, horizontal filaments perpendicular to the main tubes. To better characterize the large-scale flow structures, present before and after reconnection, we use the methods applied by Goto *et al.* [35], which consists of bandpass filtering the vorticity field. For the purpose of the present work, we found it convenient to isolate the wave numbers in the band defined by $\sqrt{2}k_f \leqslant k \leqslant 2\sqrt{2}k_f$, where $k_f = 2.3$. This value of k_f is close to the one, $k_f = \sqrt{8}$, chosen in [35]. Our own tests show that the precise value of k_f is immaterial, as long as it is small enough to filter out the small-scale features clearly seen in Figs. 2(a) and 2(b), while still capturing the change of topology due to the evolution. Using this filter, we observe that the originally horizontal tubes, parallel to the z axis in Fig. 2(c), become parallel to the y axis at later times [see Fig. 2(d)], signaling a topological transition in the vorticity field.

Between the two times shown in Figs. 2(a) and 2(b), we can observe not only changes in the large-scale vortex topology, but also the progressive appearance of small-scale vortical flow structures. At early times, we can observe the appearance of slender vortex filaments which are perpendicular to the primary vortex tubes and contain little circulation. These filaments are a well-known feature of reconnection which has already been discussed in previous studies, usually under the name of bridges [44–46]. In our simulation, they are clearly visible at $t = 15.2$; see Fig. 2(a). While the vorticity in the bridges is very much amplified at early times through vortex stretching, the role that these slender filaments have in the subsequent interaction of the main tubes during reconnection appears to be limited because they contain little circulation (see the discussion in Sec. III B). Conversely, the small-scale features that are clearly visible at later times [$t = 26.4$; Fig. 2(b)] appear to be a reproducible feature of the interaction at high Reynolds numbers; recent DNS of a pair of vortex tubes, with imposed symmetry with respect to planes P_1 and P_2 (in our terminology), also led to the formation of a similar small-scale structure, which was interpreted to be the result of a cascade [20].

The reconnection process between two vortex tubes initially at an angle $\beta = 90^\circ$, illustrated in Fig. 2, exhibits similarities with the reconnection of two tubes with symmetric initial conditions [11,20], as noted, e.g., in [37] and explained in more detail below. The dynamics leading to reconnection, however, are *not* universal. In fact, Fig. 3 shows, in a subdomain of size $5.2 \times 5.2 \times 8.5$ centered in the middle of the total domain (size $2\pi \times 2\pi \times 8\pi$), an overview of the interaction between two tubes initially at a much shallower angle, $\beta \approx 28.1^\circ$ ($b = 4$, run 11). Figure 3(a) shows that the interaction occurs over two closely paired sections of the vortex tubes, which are now much more extended in space than the sheets in Fig. 2. This is clearly illustrated by Figs. 3(c) and 3(d), which show isovorticity contours of the bandpass filtered solution for $\sqrt{2}k_F \leqslant k \leqslant 2\sqrt{2}k_F$, with $k_F = 2.3$, as shown in Figs. 2(c) and 2(d). The change in topology from Fig. 3(c) to Fig. 3(d) is similar to the above figure. However, there is a large "gap" left by the large scales. The long sheets leave behind a tangle of smaller vortices, reminiscent of the breakdown that results from the collision of two vortex rings [24,27]. This points to a dependence on the initial orientation angle, which is examined further in the following sections.

B. Evolution of two exactly or nearly perpendicular tubes: Sheet formation

Early stage and sheet formation. The reconnection process starts with the pairing of the tubes, which locally aligns the vortices in an antiparallel manner, a feature clearly observed directly from the Biot-Savart equation [9] and consistent with all previous numerical observations. The local pairing of antiparallel filaments is accompanied by a significant deformation of the vortex tubes.

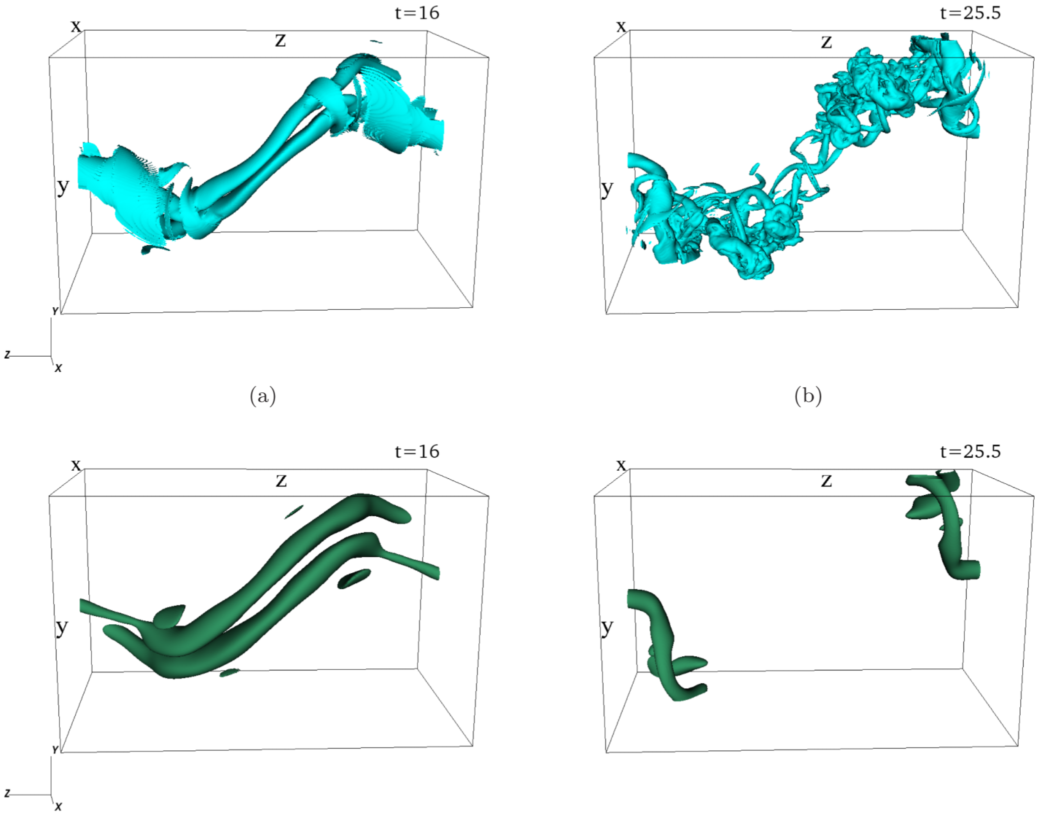

(a) (b) (c) (d)

FIG. 3. Vortex topology changes during a reconnection between tubes at an acute angle ($\beta \approx 28.1^\circ$, $b = 4$ and $\mathrm{Re}_\Gamma = 4000$, run 11 in Table I). Only a subdomain of the flow, of size $\sim 5.2 \times 5.2 \times 8.5$, is shown around the central region where the vortices interact. (a),(b) Isovorticity contours corresponding to $\omega_{th} = 2.35$ at $t = 16$, when the tubes are paired, and at $t = 25.5$, after the interaction, respectively. These panels show the generation of fine-scale vortices, similar to the collision of two antiparallel vortices [24]. (c),(d) The bandpassed vorticity field, between the wave numbers $k_< = \sqrt{2}k_f$ and $k_> = 2\sqrt{2}k_f$ (where $k_f = 2.3$), at the same times as (a) and (b). The large-scale portions of the vortex tubes at the middle of the interaction zone break down by $t = 25.5$, and the tubes reconnect at the edges of the interaction zone. The value of the isosurface ω_{th} in (c) and (d) is 0.85. Full videos of the process are available in the Supplemental Material [40].

Figures 4(a)–4(c) show isosurfaces of the vorticity magnitude for $\beta = 90^\circ$ and $\mathrm{Re}_\Gamma = 4000$ to illustrate this interaction. The three views from a perspective similar to that shown in Fig. 1(a), at $t = 17$ [Fig. 4(a)], $t = 19$ [Fig. 4(b)], and $t = 20$ (Fig. 4(c)], indicate that the nearest regions of the tubes come together and flatten into thin vortex sheets. It is important to notice that the spatial extent of the vortex sheets, in the direction of the vortex tubes, is in fact rather limited. The vortex sheets are confined in the z direction to a size smaller than that of the initial vortex cores. We also stress that the sheets do not appear to perfectly align with the P_2 ($y = 0$) plane, as it happens in the canonical problem of two initially weakly perturbed antiparallel vortex tubes, symmetric with respect to the midplane. In fact, the tilt of the sheets increases from $t = 17$ to $t = 20$. Finally, we notice that the tendency to form sheets persists at higher Reynolds numbers, for runs 4 and 5 in Table I. It thus appears that core flattening remains relevant at high Reynolds numbers, and that the argument in [22] which suggests that core flattening is limited to finite Reynolds numbers is not applicable to the problem studied here as it is based on a steady-state calculation [47].

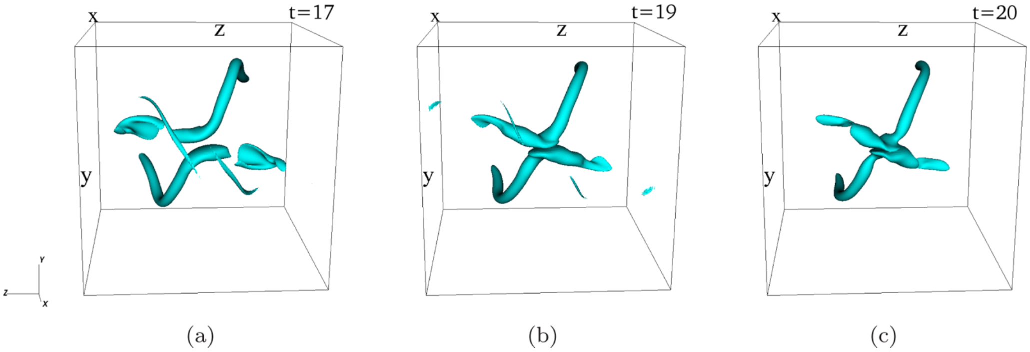

FIG. 4. Close-up view of sheet formation near the reconnection event of initially perpendicular vortex tubes (run 3, $\beta = 90^\circ$, $b = 1$, $\mathrm{Re}_\Gamma = 4000$). Isovorticity contours of the flow are shown in a subdomain of size $2.45 \times 2.45 \times 2.45$ around the central region where vorticity is the most amplified, at (a) $t = 17$ ($\omega_{th} = 3.6$), (b) $t = 19$ ($\omega_{th} = 3.8$), and (c) $t = 20$ ($\omega_{th} = 4.0$). The figure reveals the formation of a flattened region of amplified vorticity where the two tubes locally contact.

A closer inspection of the flow reveals some important differences with the well-studied highly symmetric situation. First, we note that the pairing shown in Figs. 4(a)–4(c) with the formation of vortex sheets in the regions where the vortices interact is qualitatively consistent with the simulations of [37]. As stated, the formation of sheets is a robust feature in many simulations of interacting vortex tubes, starting with an initial configuration of almost parallel counter-rotating tubes with a slight perturbation [43]. These sheets are very flat, as can be observed in Fig. 5(a), which shows a magnified view at $t = 20$, from a slightly different perspective. Figure 5(b) shows the isocontours of the z component of vorticity at the central plane, $z = 0$ [the plane P_1, as introduced in Fig. 1(a)] and clearly shows the flattened structure observed in many simulations.

This similarity, however, should be taken with care. Figure 5(a) clearly indicates that the structure of the sheets is not as flat as what had been observed in a highly symmetric problem. This is further documented by the sections of the vorticity field $|\boldsymbol{\omega}|$ in three different planes $x = x_i$, with the positions x_i being indicated by the short lines at the bottom of Fig. 5(b). The isocontours in Figs. 5(c)–5(e) indicate that the direction of the vorticity changes along the x direction, as indicated by the arrows in Figs. 5(c)– 5(e). This is in fact consistent with the general aspect of the sheets shown in Fig. 5(a). The inclinations of the vorticity in the y direction are comparably much weaker than the very visible inclination seen in Figs. 5(c)–5(e). Twisting of vortex sheets has been observed in studies of reconnecting tubes with axial flows [48]. In fact, we do observe a weak axial velocity in our problem. At the time shown in Fig. 5, the corresponding axial velocity u_z generates a component $|\omega_x| \sim |\partial_y u_z| \approx 1.5$, which is smaller than the component ω_y responsible for the tilt visible in Fig. 5, $|\omega_y| \approx 3$, and much smaller than the component $|\omega_z| \approx 8$.

We also notice that Figs. 4(a)–4(c) demonstrate that the vortex filament “bridges,” which are clearly visible at the earlier stages of the interaction when the tubes are drawn closer together [Fig. 2(a)], are still visible at $t = 17$ [Fig. 4(a)]. As the vortex tubes begin to flatten into sheets at $t = 19$ [Fig. 4(b)], these bridges become less pronounced and are no longer present at $t = 20$ [Fig. 4(c)]. Part of the reason why the bridges are less visible at later times is the increase in the vorticity threshold ω_{th} used at the three different times. The vorticity magnitude increases locally at the reconnection site where the cores become locally flattened into sheets. In fact, the bridges are concentrated in very narrow regions of space; this implies that large velocity gradients are generated, but that viscosity acts very strongly to dissipate them. For these reasons, as already stated, the

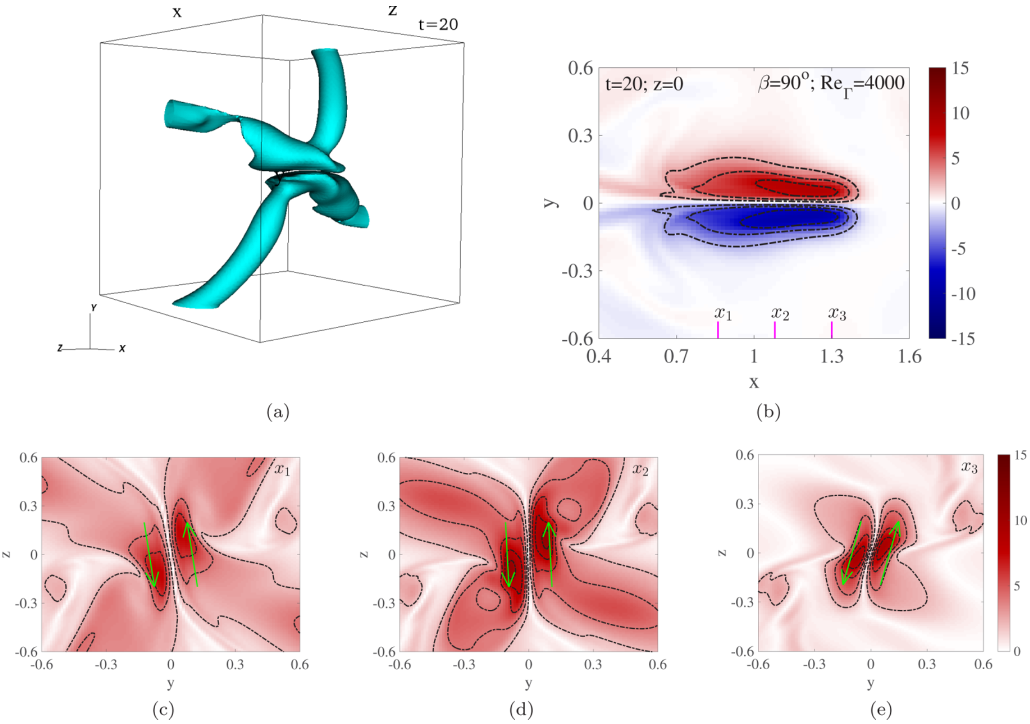

FIG. 5. Structure of the sheets formed during reconnection (run 3, $\beta = 90°$, $b = 1$, $\mathrm{Re}_\Gamma = 4000$). (a) A more detailed view of the region where the vortices interact is shown by zooming in (size of the domain shown: $1.95 \times 1.95 \times 1.95$), and rotating the domain at $t = 20$, $\omega_{th} = 4.0$ [compare with Fig. 4(c)]. (b) Cross-sectional plot of the z component of vorticity in the middle plane P_1 at $z = 0$. (c)–(e) Cross-sectional plot of the vorticity $|\boldsymbol{\omega}|$ in the horizontal planes (c) $x = x_1$, (d) $x = x_2$, and (e) $x = x_3$, with the locations being indicated in (b). The change in the orientation of the isosurfaces, clearly visible, reflects a change in the direction of the vorticity vectors along the x direction, as indicated by the arrows. The isocontour lines are separated by 2.5 in (b) and by 2 in (c)–(e).

bridges do not play any appreciable role in the reconnection dynamics and are immaterial for the present discussion.

Late stage and reconnection. The flattening of the cores into sheets is the precursor of the reconnection process. Up until the latest time, shown in Fig. 4(c), the vortex lines are not broken; they are brought together and compressed into a narrow region. The change of topology of the vortex lines, clearly illustrated in Fig. 2, occurs at a later stage through the destruction of the vortex sheets. We stress that this process is strongly constrained by the symmetry imposed, as in the previously studied case of the two initially weakly perturbed, antiparallel vortex tubes (cf. [20]). With our initial conditions, as previously noted, the sheets do not particularly align with any plane. In fact, as shown in Fig. 6, the vortex sheets strongly deform in a fully three-dimensional manner at later times. The twist of the vortex sheets, documented in Figs. 5(c) and 5(d) [see, also, Fig. 6(a) at $t = 20$], becomes even more pronounced at $t = 21.6$ [Fig. 6(b)] until the sheets, originally aligned mostly parallel to the P_2 ($y = 0$) plane, become almost vertical along the P_1 plane ($z = 0$), as shown in Fig. 6(c). The continued twisting of the vortex sheets causes them to become locally folded along both sides of the P_1 plane, leading to the formation of transverse vortex filaments. Shortly afterward, at $t = 23.2$, shown in Fig. 6(d), the main sheets in the P_1 plane are annihilated, leaving behind a complicated tangle of small-scale vortices. The results of Fig. 6 therefore show that once the vortices pair off and begin to interact, the evolution of the reconnection dynamics differs significantly from those

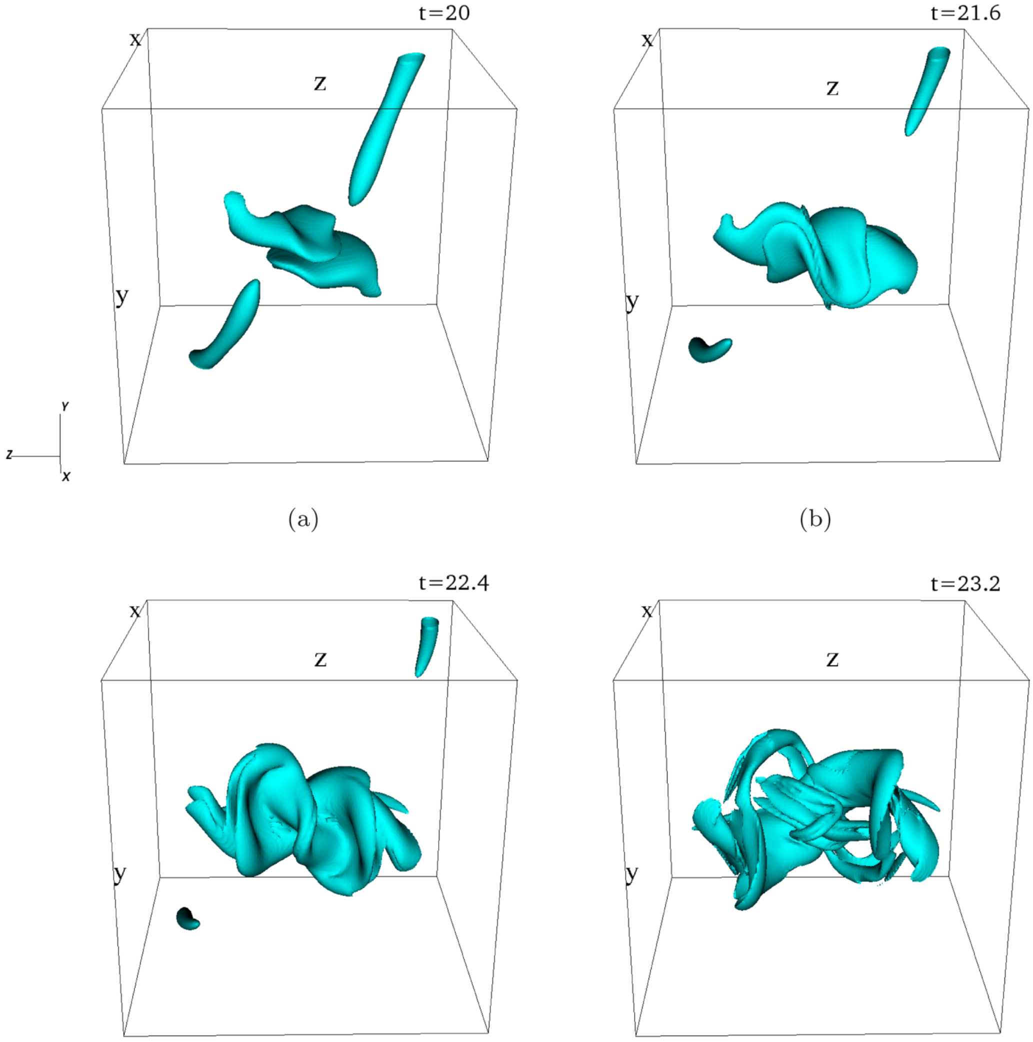

(a) (b) (c) (d)

FIG. 6. Twisting of the vortex sheets and reconnection. Vorticity magnitude isosurface for initially perpendicular vortex tubes in run 3 ($\beta = 90^\circ$, $\mathrm{Re}_\Gamma = 4000$) at three consecutive times, following the vortex sheet formation. The size of the subdomain shown is the same as in Fig. 5 ($1.95 \times 1.95 \times 1.95$). (a) After the vortex cores flatten into sheets, they become twisted as they wrap around each other. (b) The vortex sheets become folded and reorient along the $z = 0$ (P_1) plane, forming an array of transverse vortex filaments. (c) The two strong vortex sheets annihilate, leaving a tangle of small-scale vortex filaments. The last time shown, $t = 23.2$, approximately corresponds to the peak dissipation rate; see Fig. 7(b). The isovorticity contours of the flow are shown at $t = 20$ ($\omega_{th} = 4.75$), $t = 21.6$ ($\omega_{th} = 5.25$), $t = 22.4$ ($\omega_{th} = 5.60$), and $t = 23.2$ ($\omega_{th} = 6.0$). The plane P_1 ($z = 0$) separates the box shown in the middle.

obtained with a much more symmetric initial condition, such as [20], which cannot account for the twisting of the sheets. This difference may affect the formation of small-scale vortices, which form at later times, as shown in Fig. 2(b).

Evolution of global quantities. A quantitative measure of the production of small scales during the reconnection process is shown in Fig. 7 for the interaction of initially perpendicular vortex tubes

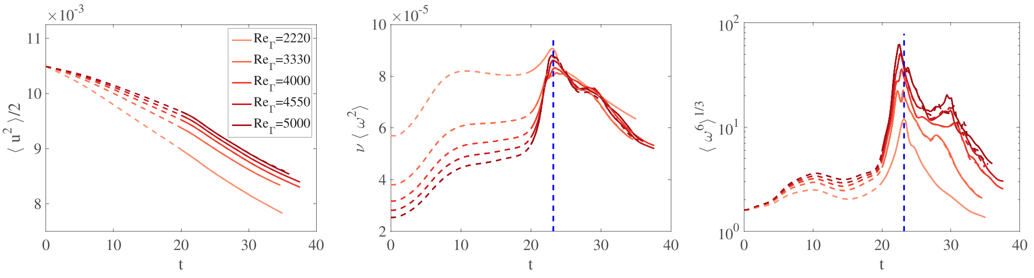

(a) (b) (c)

FIG. 7. Global dynamics for initially perpendicular vortex tubes at various Reynolds numbers. The evolution of (a) the mean kinetic energy rate $\langle \boldsymbol{u}^2 \rangle/2$, (b) the mean dissipation rate $\nu\langle \boldsymbol{\omega}^2 \rangle$, and (c) the mean sixth moment of the vorticity, $\langle \boldsymbol{\omega}^6 \rangle^{1/3}$, for runs 1–5, at fixed $\beta = 90^\circ$ and increasing values of Re_Γ. The vertical dashed line in (b) and (c) corresponds to $t = 23.2$, which is the last time shown in Fig. 6(c), and is also very close to the peak dissipation rate. The dashed (full) lines correspond to runs at low (high) resolutions.

at several Reynolds numbers. Over the entire period of the simulation, the mean kinetic energy rate, shown in Fig. 7(a), decays by less than 20%, despite the rapid increase in the mean dissipation rate, shown in Fig. 7(b). For each run, the initial mean dissipation rate decreases with a scaling of $\sim 1/\mathrm{Re}_\Gamma$ as the Reynolds number increases. It reaches a peak value at a time that is essentially independent of Re_Γ. We assume here that the peak dissipation time t_{peak} approximately coincides with the time when the small-scale vortices are most energetic, so we use this time to study the resulting small-scale structure.

Notably, the height of the peak in the dissipation rate does not vary significantly as a function of the Reynolds number. Further information on the generation of motion at small scales is provided by higher moments of the vorticity distribution. Specifically, Fig. 7(c) shows the sixth moment of the vorticity, taken to power 1/3. The sixth moment is defined as

$$\langle \boldsymbol{\omega}^{2n} \rangle = \frac{1}{V} \int_V d^3\mathbf{x} (\boldsymbol{\omega}^2)^n, \quad \text{where } n = 3. \tag{4}$$

We chose to show a moment of finite order of the vorticity distribution, rather than the maximum of the vorticity, which corresponds to the limit $n \to \infty$, as the latter is far more sensitive to finite resolution effects. Showing the moments of order $n = 2$ or $n = 4$ provides qualitatively similar information.

Since all runs share the same initial condition, the plots of $\langle \boldsymbol{\omega}^6 \rangle^{1/3}$ all start at the same initial value at 0. The peaks of the curves reach increasingly higher values with increasing Re_Γ; for the $\mathrm{Re}_\Gamma = 5000$ case, the maximum is approximately 35 times greater than the initial value. This trend reflects the strong amplification of vorticity that occurs during reconnection as the cores contact and break down to fine scales. Similar results are obtained with values of other moments of $\langle \boldsymbol{\omega}^{2n} \rangle^{1/n}$, with $n = 2$ and 4. As expected, the peak amplification for these moments grows with the order n. Note that on all plots in Fig. 7, the results of the runs at low resolution (with N_l^3 Fourier modes) are shown as dashed lines, whereas the runs at higher resolution (with N_h^3 modes, N_l and N_h both given in Table I) are represented by solid lines. The deviations between the two resolutions are small in the peak regions, even at the highest Reynolds number considered here. This gives us confidence in our numerical results. However, at $\mathrm{Re}_\Gamma = 5000$, the values of $\langle \boldsymbol{\omega}^6 \rangle^{1/3}$ at different resolutions diverge at later times (for $t \gtrsim 25$), which we interpret as a consequence of the amplification of small differences in the numerical integration of such a dynamical system with many degrees of freedom and underlying chaotic dynamics.

Evolution at $\beta \gtrsim 67.4^\circ$ ($b \leqslant 3/2$). The evolution of the global quantities for runs 3, 6, and 7, all corresponding to $\mathrm{Re}_\Gamma = 4000$, and $67.4^\circ \leqslant \beta \leqslant 90^\circ$ ($1 \leqslant b \leqslant 3/2$), is shown in Fig. 8. The initial value of the mean kinetic energy slightly decreases with β, as shown in Fig. 8(a). This can

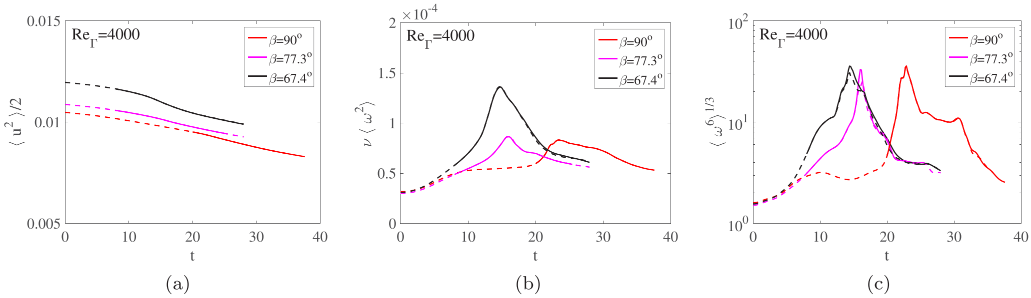

(a)

(b)

(c)

FIG. 8. Global dynamics for vortex tubes at varying initial orientation angles. The evolution of (a) the mean kinetic energy rate $\langle \boldsymbol{u}^2 \rangle/2$, (b) the mean dissipation rate $\nu\langle \boldsymbol{\omega}^2 \rangle$, and (c) the mean sixth moment of the vorticity, $\langle \boldsymbol{\omega}^6 \rangle^{1/3}$, for runs 3 ($\beta = 90^\circ$, $b = 1$), 6 ($\beta \approx 77.3^\circ$, $b = 5/4$), and 7 ($\beta \approx 67.4^\circ$, $b = 3/2$), at fixed $\mathrm{Re}_\Gamma = 4000$. The local pairing of the vortex tubes leads, in all of these cases, to the formation of vortex sheets.

be simply explained by noticing that the velocity generated by each vortex is in the azimuthal direction, and that the way the contributions from the two vortices combine actually depends on the angle β between the tubes. Over the entire runs, the kinetic energy decays by no more than approximately 20% throughout the whole run, as was the case at $\beta = 90^\circ$ (compare with Fig. 7). The main differences between the runs is indicated by the evolution of the mean dissipation rate and of $\langle \boldsymbol{\omega}^6 \rangle^{1/3}$, as shown in Figs. 8(b) and 8(c). Namely, as β decreases, the time required for these plots to reach their respective maxima also decreases. Visualization studies, comparable to what has been done in the case $\beta = 90^\circ$, show that the peaks in Figs. 8(b) and 8(c) correspond to the time at which the vortices reconnect and the tubes change topology. Notably, the reconnection dynamics look comparable when $\beta = 90^\circ$ and $\beta \approx 77.3^\circ$ ($b = 5/4$), with the prominent formation of vortex sheets as illustrated in Fig. 4. The major difference between these two cases comes from the time at which the peaks develop; see Figs. 8(b) and 8(c). This difference can be qualitatively understood from the observation that when β decreases, the vortex tubes are initially closer to being antiparallel, and it therefore takes less time for them to locally align in an antiparallel manner and initiate the reconnection process. As explained earlier, this early phase can be captured with the Biot-Savart dynamics.

Contrary to the peaks of $\langle \boldsymbol{\omega}^6 \rangle^{1/3}$ shown in Fig. 8(c), which are approximately constant, the peak energy dissipation rate is approximately twice as large for the configuration where $\beta \approx 67.4^\circ$ ($b = 3/2$) than for $\beta = 90^\circ$ ($b = 1$) or $\beta \approx 77.3^\circ$ ($b = 5/4$). Visualization in the former case also reveals the transient presence of vortex sheets when the tubes come together. The evolution, however, qualitatively differs from what was shown in Fig. 4, as the sheets do not stay close to one another. We view this regime as a transition towards the dynamics occurring at smaller values of β, which will be discussed in the following section.

C. Evolution at $\beta \leqslant 53.1^\circ$ ($b \geqslant 2$): Short-wavelength instability

As the initial condition is varied to increase the alignment of the tubes (i.e., $\beta \to 0$), the interactions close to the reconnection event become very different to what was shown for initially perpendicular tubes in Fig. 4. This is illustrated by Fig. 9, which shows the development of the interaction between the vortex tubes for run 11 with $\beta \approx 28.1^\circ$ ($b = 4$) and $\mathrm{Re}_\Gamma = 4000$. Because the angle between the two tubes is much smaller than the initially perpendicular case ($b = 1$), the two tubes align, overlap, and interact over a significantly larger extent that is much larger than the initial vortex core size. This is clearly visible in the left column of Fig. 9, as the extent of the vortices in the z direction is much larger than in the x and y directions. In fact, as the flow evolves from $t = 15.6$ [Figs. 9(a) and 9(d)] to $t = 20.4$ [Figs. 9(b) and 9(e)], the vortices develop an instability over a wavelength comparable to the size of the core. As the instability further evolves,

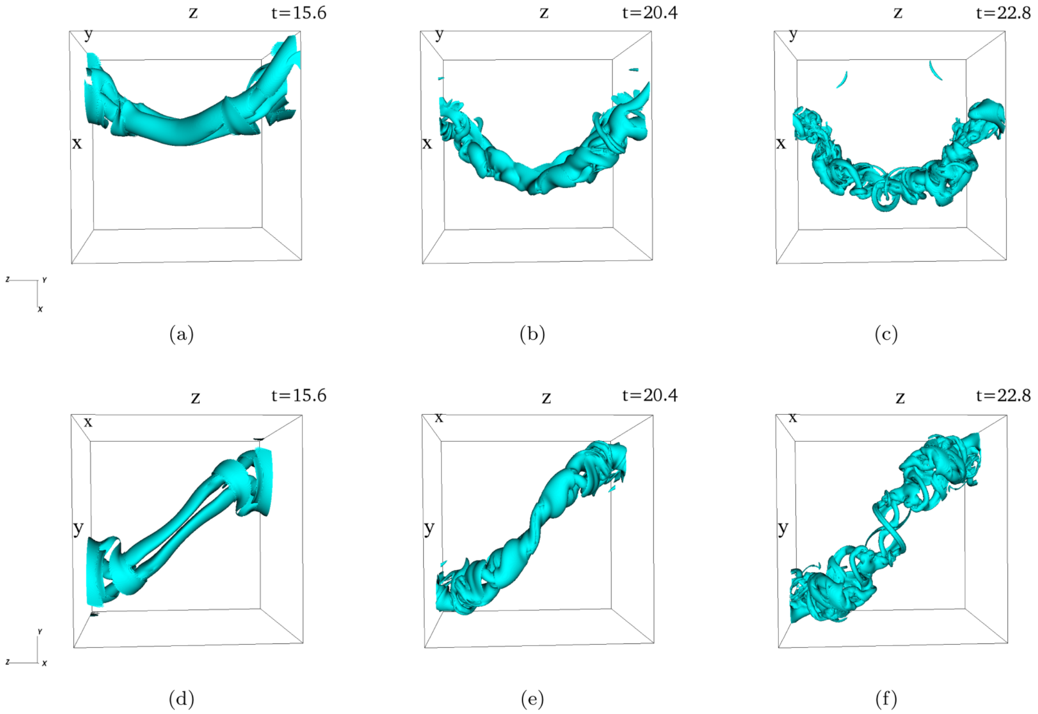

FIG. 9. Interaction and breakdown of nearly antiparallel vortex tubes. The evolution of the vorticity magnitude isosurface for run 11 ($\beta \approx 28.1^\circ$, $b = 4$, $\mathrm{Re}_\Gamma = 4000$). Only a cubic subdomain, $[-2.6, 2.6]^3$, surrounding the regions where the vortices interact is shown. The isosurfaces of the vorticity field are shown at $t = 15.6$ (left), $t = 20.4$ (center), and $t = 22.8$ (right); the upper row shows the top view and the bottom row shows the front view. The thresholds are $\omega_{th} = 2.5$ ($t = 15.6$), 3.2 ($t = 20.4$), and 3.6 ($t = 22.8$). The latest time shown corresponds to the peak dissipation rate.

many small-scale vortices develop [Figs. 9(c) and 9(f)] through the mutual stretching and straining of perpendicular vortices, which is mediated by the elliptical instability [24].

To characterize the evolution of the solution leading to the generation of small scales of motion, Fig. 10 provides information on the vorticity in the tubes by showing the z component ω_z in two planes, away from the symmetry plane P_1 ($z = 0$), at $z \approx 0.24$ (upper row) and $z \approx 0.47$ (lower row), at three times: $t = 17.2$ (left column), $t = 18.0$ (middle column), and $t = 18.8$ (right column). In the plane P_1, the solution at these three times remains symmetric with respect to y, with a characteristic vortex dipole shape, without any tendency to develop the sheetlike structure, clearly documented for $\beta = 90^\circ$ in Figs. 4 and 5. In the case of vortices at $\beta = 28.1^\circ$, Fig. 10 shows a clear deformation of the cores, where the upper core (positive vorticity) wraps around the lower core, with a thin layer being pulled down. These effects, also documented in the Supplemental Material of [24], become more pronounced when z and t increase. This twisting of the vortices is accompanied by the concentration of the vorticity distribution at certain places, away from the region of contact between the two tubes. Figure 10 demonstrates that the solution with paired vortices, which could conceivably be approximated as an extended dipole along the z axis perpendicular to the figure [11], is not stable due to the evolution of the degrees of freedom of the vortex core. The drift in the structure of the vorticity distribution could be conceivably interpreted as a manifestation of the known instability mechanisms of two paired vortex tubes, discussed many times [24,26]. The breaking of the translational symmetry along the z axis in the problem of two vortices at $\beta = 28.1^\circ$, however, leads to a major difference with the case studied in [24], where the development of small

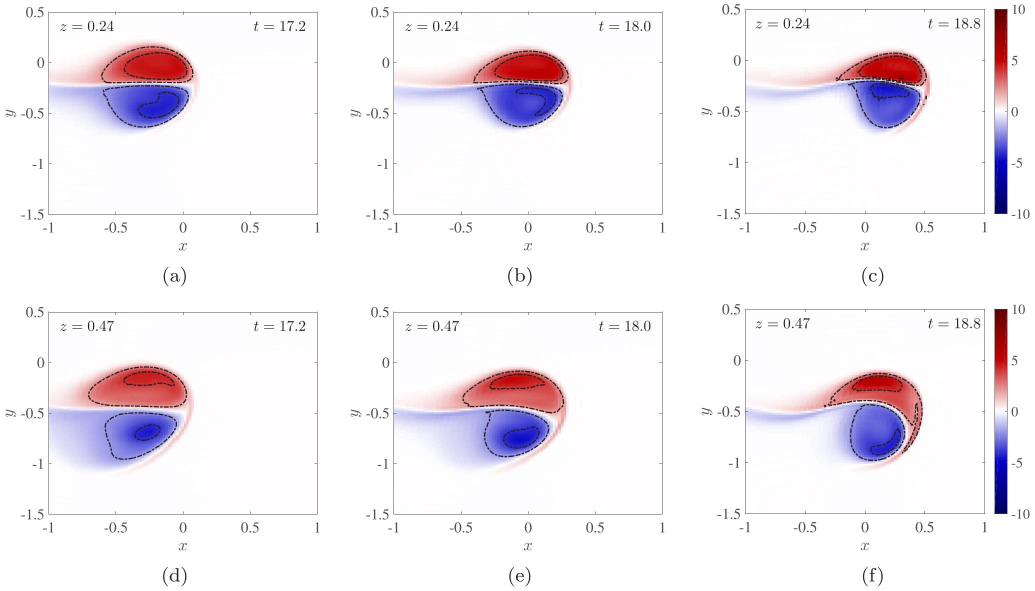

(a) (b) (c)

(d) (e) (f)

FIG. 10. Vortex core structure at two positions, $z \approx 0.12$ (upper row) and $z \approx 0.23$ (lower row). The times shown are intermediate between the two first times shown in Fig. 9, and correspond to the phase where small-scale structures begin to form. The upper core wraps around the lower core, the more so as the plane is further away from the center (z increases). In addition, (f) begins to show the formation of regions where vorticity gets more intense, as was found in the case for two antiparallel filaments [24].

scales was due solely to the development of the elliptic instability [24]. The interplay between the intrinsic instability and the more complicated initial value, as shown in Figs. 9 and 10, is difficult to disentangle, although some of the features in the two problems are qualitatively similar. We also observed a weak axial velocity along the vortex tubes, which is known to modify the development of the elliptic instability [49]. In any event, in the case of vortices originally at $\beta = 28.1^\circ$, the precursor of reconnection definitely does not involve pairs of vortex sheets.

The results shown in this section sharply contrast with those shown in Sec. III B for $\beta \gtrsim 67.4^\circ$ ($b < 3/2$). In fact, we can distinguish between two very different qualitative behaviors. For $\beta \gtrsim 67.4^\circ$ ($b < 3/2$), the interaction of the vortex tubes leads to the localized formation of thin vortex sheets that are limited to the interaction zone. In contrast, for $\beta \lesssim 53.1^\circ$ ($b \geqslant 2$), the interaction of the two vortex tubes leads to an interaction similar to that shown in Fig. 9, where perpendicular, fine-scale filaments arise throughout large areas of the domain. We stress the qualitative resemblance of the production of small scales in this figure with the results shown in [24,27]. We recall that the flow corresponding to run 7 ($\beta \approx 67.4^\circ$, $b = 3/2$) does lead to the development of sheets, but the interaction mechanism ultimately differs from those shown in Figs. 4 and 9 because even if small-scale perpendicular filaments arise they come in small numbers and do not significantly interact with each other.

Figure 11 shows the time dependence of the kinetic energy of the runs [Fig. 11(a)], the dissipation rate [Fig. 11(b)], and the sixth moment of vorticity, $\langle \boldsymbol{\omega}^6 \rangle^{1/3}$, for runs 8–11, where $\beta \leqslant 53.1^\circ$ ($b \geqslant 2$) and $\mathrm{Re}_\Gamma = 4000$. We have indicated by a cross in Figs. 11(b) and 11(c) the latest time corresponding to the visualization in Fig. 9(c), which approximately coincides with the peak dissipation rate. As was the case for the runs at $\beta \gtrsim 67.4^\circ$ ($b \leqslant 3/2$) (see Fig. 8), the time of the peak dissipation, t_{peak}, varies with β. Figure 11(b) shows that t_{peak} increases when β decreases. It should be kept in mind that the time at which the interaction occurs is a consequence of the pairing process, which depends on the precise geometry of the problem and, more specifically, on the angle β between the

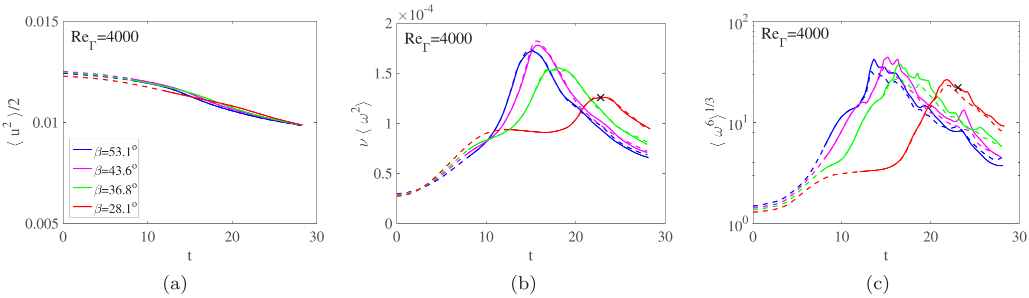

FIG. 11. Global dynamics for vortex tubes initially oriented at shallow angles. The evolution of (a) the mean kinetic energy rate $\langle \boldsymbol{u}^2 \rangle/2$, (b) the mean dissipation rate $\nu\langle \boldsymbol{\omega}^2 \rangle$, and (c) the mean sixth moment of the vorticity, $\langle \boldsymbol{\omega}^6 \rangle^{1/3}$, for runs 8 ($\beta \approx 53.1^\circ$, $b = 2$), 9 ($\beta \approx 43.6^\circ$, $b = 5/2$), 10 ($\beta \approx 36.8^\circ$, $b = 3$), and 11 ($\beta \approx 28.1^\circ$, $b = 4$), at fixed $\mathrm{Re}_\Gamma = 4000$.

vortex tubes. As the tubes become more parallel, it takes a longer time for the interaction between the tubes to initiate. In the limit of perfectly antiparallel filaments, this time becomes the time necessary for instabilities to grow, as observed in [24]. It depends on the amount of noise initially and it can be much longer than the time $t \approx 25$ for run 11 ($\beta \approx 28.1^\circ$, $b = 4$). In fact, we checked that the triggering of the elliptic instability, leading to the strong interaction between two antiparallel vortex tubes, is delayed when decreasing the amplitude of the noise added to the solution. This is consistent with the intuitive notion that the interaction leading to turbulence starts with an exponential growth of a small perturbation of the two initially antiparallel vortex tubes.

Interestingly, we also notice that the value of the peak dissipation rate tends to decrease when β decreases, for $\beta \lesssim 43.6^\circ$ ($b \gtrsim 5/2$). A similar trend is also observed in the sixth moment [see Fig. 11(c)], as well as for the fourth and eighth moments (not shown). Contrary to runs at higher values of β, we observe a stronger difference between the runs at low resolution (with N_l Fourier modes, shown as dashed lines) and the runs at a higher resolution (with N_h Fourier modes, shown as full lines). This indicates stronger resolution requirements for these runs.

D. Discussion

Whereas the interaction between vortex tubes always leads to reconnection, i.e., to a change of topology of the vortex lines, the mechanisms involved when the initial conditions are close to antiparallel ($\beta \lesssim 33.7^\circ$ or $b > 3/2$; see Sec. III C) appear to qualitatively differ from what is observed when the vortices are closer to being perpendicular ($\beta \gtrsim 33.7^\circ$ or $b < 3/2$) as discussed in Sec. III B. The dynamics observed in the former case are very reminiscent of what was observed during the interaction of two initially antiparallel vortex tubes [24,27]. The qualitative similarity between reconnection when $b = 4$, occurring through the annihilation of a large fraction of the two locally antiparallel tubes, clearly shown in Figs. 3 and 9, and the dynamics resulting from the collision between two vortex rings [24], is an important aspect of our work.

This configuration of two antiparallel tubes formally corresponds to $\beta \to 0^\circ$ ($b \to \infty$). In fact, the behaviors of the mean kinetic energy, dissipation rate, and sixth moment of vorticity in runs with initially weakly perturbed antiparallel vortex tubes (see Fig. 12) are very comparable to that shown for $\beta = 28.1^\circ$. Still, as explained above, the major difference between the configuration at a weak, but finite angle ($\beta > 0$) and that of two antiparallel vortex tubes ($\beta = 0$) comes from the breaking of translational symmetry along the z axis when $\beta > 0$. This breaking of symmetry acts as a perturbation to the state of parallel vortices, which is the starting point for the dynamics of the core, and for a systematic deviation between a simple translation of a vortex dipole, as illustrated in Fig. 10. In fact, in the case of antiparallel tubes $\beta = 0$, the development of small scales is entirely due to the growth of an instability. This can be clearly seen in Figs. 12(b) and 12(c), which compares

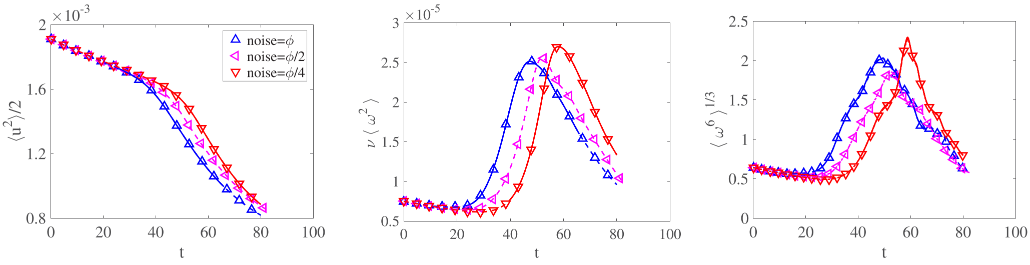

(a) (b) (c)

FIG. 12. Global dynamics for initially antiparallel vortex tubes with various noise levels. The evolution of (a) the mean kinetic energy rate $\langle \boldsymbol{u}^2\rangle/2$, (b) the mean dissipation rate $\nu\langle\boldsymbol{\omega}^2\rangle$, and (c) the mean sixth moment of the vorticity, $\langle\boldsymbol{\omega}^6\rangle^{1/3}$, for run 12 with varying noise amplitudes where $\beta = 0^\circ$ and $\mathrm{Re}_\Gamma = 4000$. The results shown here correspond to a resolution of $192^2 \times 768$. Results at higher resolution, up to $320^2 \times 1280$, do not differ appreciably from those shown here. A movie showing the evolution of the solution for the run with the highest level of noise can be found in the Supplemental Material [40].

three simulations with three different noise levels, obtained from a weak level (upward-triangles), half its value (left-pointing triangles), and a quarter of its value (downward triangles). The time where the dissipation rate peaks clearly depends on the destabilization of the initial noise amplitude: we observe a logarithmic dependence of this time, consistent with the intuitive notion that the first stage of the interaction comes from the exponential growth of an unstable perturbation, through the elliptic instability.

This signals a clear qualitative difference between this configuration, where the interaction between the tubes leads to the annihilation of increasingly larger parts of overlapping tubes, and that obtained for $\beta > 67.4^\circ$ ($b < 3/2$), where intense, extremely thin vortex sheets form before a reconnection event [11,17,20]. Both types of events lead to the formation of small-scale structures, albeit through different dynamics. We postulate that for sufficiently large Reynolds numbers and small values of β, reconnection is overtaken by the mutual annihilation of the two tubes through the elliptical instability. This is because the elliptical instability requires the strain to be aligned along the vortex core to begin to act (hence it barely acts for $\beta = 90^\circ$), but its growth rate is much larger than that of the Crow instability that leads to reconnection [24]. Even if the overall dynamics preceding reconnection appear to depend on the initial condition, the late stage of the interaction leads, at high enough Reynolds numbers in all cases studied, to an intense generation of small scales, plausibly through a cascade as demonstrated in the case of parallel tubes in [24]. Based on these observations, we postulate that this cascade, through the generation of perpendicular, small-scale vortices, may in fact be universal [19,35], independently of the initial conditions.

IV. SUMMARY AND CONCLUSION

In this work, we have investigated the interaction between two initially straight, counter-rotating vortex tubes oriented at an angle β. We systematically varied β, and hence the geometry of the initial flow configuration, and let the flow evolve. In all cases, we observe a change in topology of the vortex lines and the production of perpendicular small-scale vortices. The main result of our study is that the dynamics which result in this outcome strongly depend on the initial orientation of the interacting tubes.

When the tubes are initially almost perpendicular to each other ($\beta \approx 90^\circ$), the interacting vortex tubes locally contact where they overlap, flattening into a pair of intense, slender vortex sheets. This resembles the classically studied reconnection found in the case of a pair of straight vortex tubes with a perturbation symmetric with respect to the plane separating the two vortices [11,15–20,42,43], and which involves the flattening of the vortex tubes into intense, slender vortex sheets on either side of the symmetry plane. The underlying symmetries in the flow appear to be consistent with the eigenmodes corresponding to the long-wavelength (Crow) instability [12] and can be adequately captured in a flow with imposed symmetries. The subsequent breakdown of the tubes, which ultimately leads to abundant formation of small scales [20], involves the twisting of the vortex lines resulting from the approximate nature of the symmetry.

However, when the angle between the two filaments is initially acute, we observe a breakdown mechanism that is very different and qualitatively consistent with that of Refs. [24,27], with the formation of abundant small-scale vortices perpendicular to the original tubes, which effectively transfers more energy to the small scales. It is difficult to disentangle the role of the antisymmetric elliptical instability in the process, given the obvious difference with the conceptually simpler case of two antiparallel tubes. Nonetheless, the evolution of the tubes cannot be captured by assuming the mirror image symmetry, as done in many earlier studies.

It is interesting to contrast this study with the nonuniversal aspects of vortex reconnection in superfluids, documented in [33], which rest on the precise geometry of the filament pair when the vortices reconnect. The nonuniversality documented in the present work rests on the dynamics of the vortex cores, which are responsible for the onset and dynamics of the elliptic instability. The Reynolds number also appears to be an important parameter in the reconnection of vortex tubes in classical fluids, a flow parameter without an analog in superfluids.

While the early stages of vortex interactions do not appear to lead to a universal reconnection scenario, we observe that the interaction between two vortex tubes leads, in seemingly different ways, to a proliferation of small-scale flow structures. In the problem considered here, when $\beta \approx \pi/2$, the small scales form after the sheets have annihilated, as observed in [20]. When the tubes are better aligned in an antiparallel manner, the formation of small-scale vortex structures via a cascade occurs as soon as the vortices come together [24]. The idea that iterative mechanisms may lead to the formation of a cascade has been suggested for theoretical reasons [19,50]. The numerical results presented here show the formation of very small scales, in a way reminiscent of what was observed during the interaction of two vortex tubes [24]. An interesting question for future work will be to understand whether the mechanism leading to the proliferation of small-scale vortices is universal, based on the physical mechanisms discussed in [24]. The possibility that such a cascade scenario may lead to a singularity, as already postulated [19,50,51], and the precise nature of the $\mathrm{Re}_\Gamma \to \infty$ limit [52] also deserve further attention.

ACKNOWLEDGMENTS

R.O.M. thanks the Research Computing Data Core (RCDC) at the University of Houston for providing computing resources. This research was funded by the National Science Foundation through the Harvard Materials Research Science and Engineering Center Grant No. DMR-2011754, and through the Division of Mathematical Sciences Grant No. DMS-1715477. M.P.B. is an investigator of the Simons Foundation. A.P. acknowledges financial support from the IDEXLYON project (Contract No. ANR-16-IDEX-0005) under the University of Lyon auspices, as well as from the project TILT from the French Agence Nationale de la Recherche, under Contract No. ANR-20-CE30-0035.

APPENDIX: SPECTRA

In this Appendix, we show the energy spectra of the solutions at times where the resolution requirements are the most severe, namely, close to the time where energy dissipation peaks. Figures 13(a) and 13(b) show the spectra for runs at $\beta = 90^\circ$, for $\mathrm{Re}_\Gamma = 5400$ and $\mathrm{Re}_\Gamma = 4000$, respectively; the latter run corresponds to the solution, visualized in Figs. 2, 4, 5, and 6. Additionally, Fig. 13(c) shows the spectra of run 11, presented in Figs. 3 and 9. Last, Fig. 13(d) shows the run corresponding to $\beta = 0^\circ$, with the largest initial perturbation (run 12A).

For all spectra, the energy dissipation is shown as an inset, with a vertical bar indicating the time corresponding to the spectra. We also show the reference Kolmogorov $k^{-5/3}$ spectrum. At the

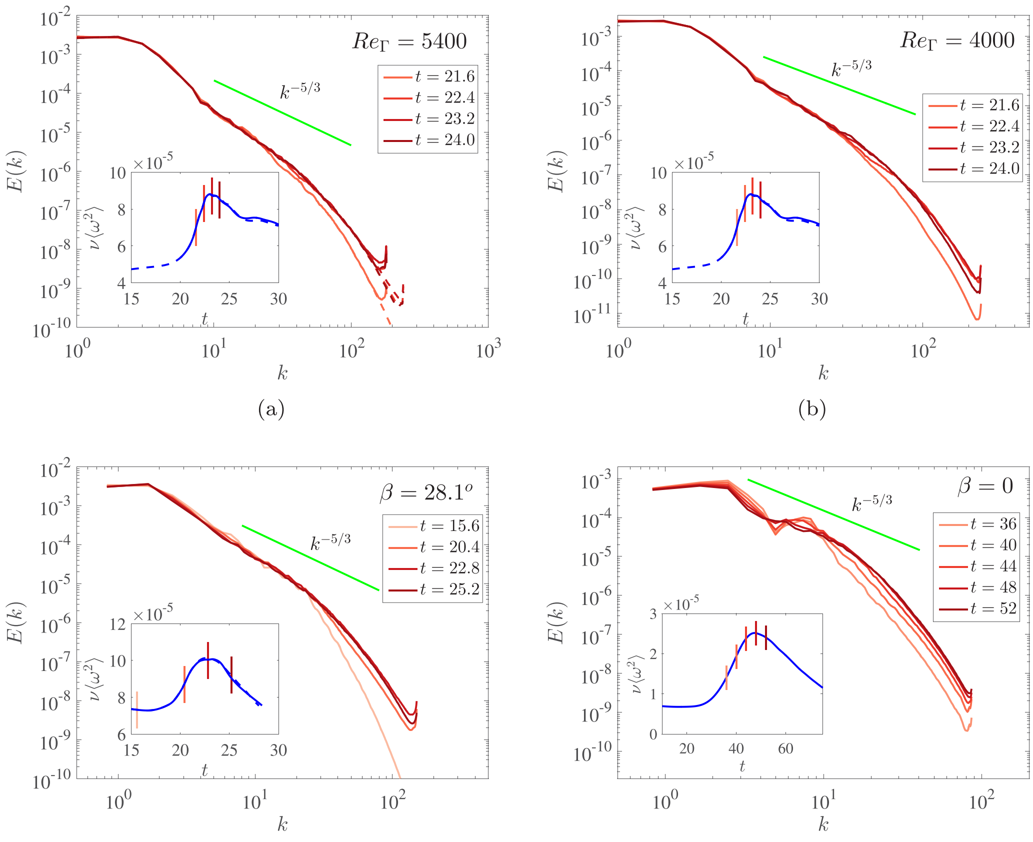

(a) (b) (c) (d)

FIG. 13. Spectra of the solutions close to the peak of dissipation. The inset shows the energy dissipation, with the bars indicating the time at which the solution is shown. (a) Run 5 ($\mathrm{Re}_\Gamma = 5400$, $\beta = 90°$), (b) run 3 ($\mathrm{Re}_\Gamma = 4000$, $\beta = 90°$), (c) run 11 ($\mathrm{Re}_\Gamma = 4000$, $\beta = 28.1°$), and (d) run 12A ($\mathrm{Re}_\Gamma = 4000$, $\beta = 0°$). For reference, the Kolmogorov $k^{-5/3}$ spectrum is indicated on all panels.

relatively low Reynolds number used here, only the run at $\beta = 0°$ exhibits a clear indication of a $k^{-5/3}$ spectrum, consistent with [24]. A compensation of the actual spectrum by $\epsilon^{2/3}k^{-5/3}$ would lead to a constant of order 1, consistent with known values of the Kolmogorov constant.

---

[1] P. G. Saffman, Dynamics of vorticity, J. Fluid Mech. **106**, 49 (1981).

[2] P. R. Schatzle, An experimental study of fusion of vortex rings, Ph.D. thesis, California Institute of Technology, 1987.

[3] P. G. Saffman, *Vortex Dynamics* (Cambridge University Press, Cambridge, 1992).

[4] Susumu Goto, Coherent structures and energy cascade in homogeneous turbulence, Prog. Theor. Phys. Suppl. **195**, 139 (2012).

[5] AKM Fazle Hussain, Coherent structures and turbulence, J. Fluid Mech. **173**, 303 (1986).

[6] M. W. Scheeler, W. M. van Rees, H. Kedia, D. Kleckner, and W. T.M. Irvine, Complete measurement of helicity and its dynamics in vortex tubes, Science **357**, 487 (2017).

[7] G. K Batchelor, *An Introduction to Fluid Dynamics* (Cambridge University Press, Cambridge, 1970).

[8] A. Leonard, Vortex methods for flow simulation, J. Comput. Phys. **37**, 289 (1980).

[9] E. D. Siggia, Collapse and amplification of a vortex filament, Phys. Fluids **28**, 794 (1985).
[10] W. T. Ashurst and D. I. Meiron, Numerical Study of Vortex Reconnection, Phys. Rev. Lett. **58**, 1632 (1987).
[11] A. Pumir and R. M. Kerr, Numerical Simulation of Interacting Vortex Tubes, Phys. Rev. Lett. **58**, 1636 (1987).
[12] S. C. Crow, Stability theory for a pair of trailing vortices, AIAA J. **8**, 2172 (1970).
[13] E. D. Siggia and A. Pumir, Incipient Singularities in the Navier-Stokes Equations, Phys. Rev. Lett. **55**, 1749 (1985).
[14] A. Pumir and E. D. Siggia, Vortex dynamics and the existence of solutions to the Navier-Stokes equations, Phys. Fluids **30**, 1606 (1987).
[15] A. Pumir and E. D. Siggia, Collapsing solutions to the 3d Euler equations, Phys. Fluids **2**, 220 (1990).
[16] M. J. Shelley, D. I. Meiron, and S. A. Orszag, Dynamical aspects of vortex reconnection of perturbed antiparallel vortex tubes, J. Fluid Mech. **246**, 613 (1993).
[17] R. M. Kerr, Evidence for a singularity of the three-dimensional incompressible Euler equations, Phys. Fluids A **5**, 1725 (1993).
[18] T. Y. Hou and R. Li, Dynamic depletion of vortex stretching and non-blowup of the 3-d incompressible euler equations, J. Nonlinear Sci. **16**, 639 (2006).
[19] M. P. Brenner, S. Hormoz, and A. Pumir, Potential singularity mechanism for the Euler equations, Phys. Rev. Fluids **1**, 084503 (2016).
[20] J. Yao and F. Hussain, A physical model of turbulence cascade via vortex reconnection sequence and avalanche, J. Fluid Mech. **883**, A51–1–36 (2020).
[21] S. Hormoz and M. P. Brenner, Absence of singularity of interacting vortex filaments, J. Fluids Mech. **707**, 191 (2012).
[22] H.K. Moffatt and Y. Kimura, Towards a finite time singularity of the Navier-Stokes equations Part 1. Derivation and analysis of dynamical systems, J. Fluid Mech. **861**, 930 (2019).
[23] W. M. van Rees, F. Hussain, and P. Koumoutsakos, Vortex tube reconnection at $\mathrm{Re} = 10^4$, Phys. Fluids **24**, 075105 (2012).
[24] R. McKeown, R. Ostilla-Mónico, A. Pumir, M. P. Brenner, and S. M. Rubinstein, Turbulence generation through an iterative cascade of the elliptical instability, Sci. Adv. **6**, eaaz2717 (2020).
[25] T. T. Lim and T. B. Nickels, Instability and reconnection in the head-on collision of two vortex rings, Nature (London) **357**, 225 (1992).
[26] T. Leweke, S. Le Dizès, and C. H. K. Williamson, Dynamics and instabilities of vortex pairs, Annu. Rev. Fluid Mech. **48**, 507 (2016).
[27] R. McKeown, R. Ostilla-Mónico, A. Pumir, M. P. Brenner, and S. M. Rubinstein, Cascade leading to the emergence of small scale structures in vortex ring collisions, Phys. Rev. Fluids **3**, 124702 (2018).
[28] C. Y. Tsai and S. E. Widnall, The stability of short waves on a straight vortex filament in a weak externally imposed strain field, J. Fluid Mech. **73**, 721 (1976).
[29] D. W. Moore and P. G. Saffman, The instability of a straight vortex filament in a strain field, Proc. R. Soc. London Ser. A **346**, 413 (1975).
[30] B. J. Bayly, Three-Dimensionality of Elliptical Flow, Phys. Rev. Lett. **57**, 2160 (1986).
[31] R. R. Kerswell, Elliptic instabilities, Annu. Rev. Fluid Mech. **34**, 83 (2002).
[32] M.G. Linton, R. B. Dahlburg, and S. K. Antiochos, Reconnection of twisted flux tubes as a function of contact angle, Astrophys. J. **555**, 905 (2001).
[33] A. Villois, D. Proment, and G. Krstulovic, Universal and nonuniversal aspects of vortex reconnections in superfluids, Phys. Rev. Fluids **2**, 044701 (2017).
[34] Y. Kimura and H. K. Moffatt, Reconnection of skewed vortices, J. Fluid Mech. **751**, 329 (2014).
[35] S. Goto, Y. Saito, and G. Kawahara, Hierarchy of antiparallel vortex tubes in spatially periodic turbulence at high Reynolds numbers, Phys. Rev. Fluids **2**, 064603 (2017).
[36] C. L. Fefferman, Existence and smoothness of the Navier-Stokes equations (Clay Mathematical Institute, Cambridge, MA, 2006).
[37] O. Boratav, R. B. Pelz, and N. J. Zabusky, Reconnection in orthogonally interacting vortex tubes: Direct numerical simulations and quantifications, Phys. Fluids **4**, 581 (1992).

[38] J. Yao and F. Hussain, Universal scaling for vortex reconnection in classical and quantum fluids, Bull. Am. Phys. Soc. (2020), https://meetings.aps.org/Meeting/DFD20/Session/P18.1.

[39] A. Pumir, A numerical study of pressure fluctuations in three-dimensional incompressible homogeneous turbulence, Phys. Fluids **6**, 2071 (1994).

[40] See Supplemental Material at http://link.aps.org/supplemental/10.1103/PhysRevFluids.6.074701 for supplementary videos.

[41] F. Laporte and A. Corjon, Direct numerical simulations of the elliptic instability of a vortex pair, Phys. Fluids **12**, 1016 (2000).

[42] R. M. Kerr and A. K. M. F. Hussain, Simulations of vortex reconnection, Physica D **37**, 474 (1989).

[43] R. M. Kerr, The growth of vorticity moments in the Euler equations, Proc. IUTAM **7**, 49 (2013).

[44] S. Kida and M. Takaoka, Bridging in vortex reconnection, Phys. Fluids **30**, 2911 (1987).

[45] M. V. Melander and F. Hussain, *Cut-and-connect of Two Antiparallel Vortex Tubes* (Center for Turbulence Research, Stanford University, California, 1988).

[46] S. Kida and M. Takaoka, Vortex reconnection, Annu. Rev. Fluid Mech. **26**, 169 (1994).

[47] H.K. Moffatt, S. Kida, and K. Ohkitani, Stretched vortices: The sinews of turbulence; Large-Reynolds-number asymptotics, J. Fluid Mech. **259**, 241 (1994).

[48] P. McGavin and D. I. Pontin, Reconnection of vortex tubes with axial flow, Phys. Rev. Fluids **4**, 024701 (2019).

[49] L. Lacaze, K. Ryan, and S. Le Dizès, Elliptic instability in a strained batchelor vortex, J. Fluid Mech. **577**, 341 (2007).

[50] T. Tao, Finite time blowup for an averaged three-dimensional Navier-Stokes equation, J. Am. Math. Soc. **29**, 601 (2016).

[51] J. Yao and F. Hussain, On singularity formation via viscous vortex reconnection, J. Fluid Mech. **888**, R2 (2020).

[52] P. Constantin, Note on loss of regularity for solutions of the 3-d incompressible Euler and related equations, Commun. Math. Phys. **104**, 311 (1986).